Computational Modelling of Electro-Mechanical Coupling in the Atria and its Changes during Atrial Fibrillation

Sofia Monaci[1*], David Nordsletten[1] and Oleg Aslanidi[1]

[1] School of Biomedical Engineering & Imaging Sciences, King's College London, UK

[*]sofia.monaci@kcl.ac.uk

Abstract. Atrial fibrillation (AF) is a very common, multifaceted disease that affects atrial structure as well as electrophysiological and biomechanical function. However, the mechanistic links between structural and functional factors underlying AF are poorly understood. To explore these mechanisms, a 3D atrial electro-mechanical (EM) model was developed that includes 3D atrial geometry based on the Visible Female dataset, rule-based fibre orientation, CRN human atrial electrophysiology model and activation-based mechanical contraction model. Electrical activation in the 3D atria was simulated under control condition and two AF scenarios: sinus rhythm (SR), functional re-entry in the right atrium (RA) and structural re-entry around fibrotic patches in the left atrium (LA). Fibrosis distributions were obtained from patient LGE MRI data. In both AF scenarios, re-entrant behaviours led to substantial reductions in the displacement at peak contraction compared to SR. Specifically, high-frequency re-entry led to a decrease in maximal displacement from 6.8 to 6.1 mm in the posterior RA, and a larger decrease from 7.8 to 4.5 mm in the LA in the presence of fibrotic patches. The simulated displacement values agreed with available clinical data. In conclusion, the novel model of EM coupling in the 3D human atria provided new insights into the mechanistic links between atrial electrics and mechanics during normal activation and re-entry sustaining AF. Re-entry in the RA and LA resulted in weaker contractions compared to SR, with additional effect of fibrosis on the atrial wall stiffness further reducing the contraction.

Keywords: atrial fibrillation, electro-mechanical coupling, sinus rhythm, re-entry, fibrosis, mechanical contraction.

1 Introduction

Atrial Fibrillation (AF), one of the most common forms of arrhythmia [1], is characterized by a significant increase of the atrial rate (up to 400-600 beats per minute) and electrical desynchronization, which causes the atria to quiver instead of contracting. In a healthy heart, the electrical activity of the atria is driven by action potentials (APs) generated in the Sino-atrial node (SAN), which then spread as waves through all chambers of the heart. This provides basis for electrical coupling and synchronization of the myocardium and allows various regions of the heart, from the atria to the ventricles, to inflate and contract as a unit. However, during AF, the desynchronization of electrical activity causes asynchronous contraction of cardiac fibers and a reduction in the atrial mechanical work, affecting blood flow and cardiac output. In the long term, this can predispose to stroke, heart failure and sudden death, increasing the rates of mortality and morbidity associated with AF [2, 3].

The complexity of AF and the multiple challenges in understanding and treating this self-sustained and treatment-resistant condition warrant the use of multi-disciplinary and multi-physics approaches to elucidate its complex mechanisms. Over the years, computational modelling has led to important insights into the mechanisms of AF, primarily focusing on the electrophysiological (EP) aspects. Thus, atrial models facilitated the understanding of the main drivers of AF, high-frequency re-entrant electrical waves called rotors [4], and the mechanisms of their initiation and sustenance. Despite of the importance of the excitation-contraction coupling for an efficient pumping and mixing of the blood, very few studies have considered electro-mechanical processes during AF. Understanding how the presence of rotors and underlying structural and functional factors affect atrial mechanics is crucial for dissecting the mechanistic links between the EP and mechanical atrial functions, and can provide biomarkers for the quantification of AF state. Specific factors that can influence atrial EP function, as well as atrial stiffness and contractions, include major effects of fibrotic tissue on the rotor behaviour – which have been characterized recently [5, 6] .

This study aims to couple electrical and mechanical processes using the 3D atrial models to understand how electrical drivers for AF influence contraction of atrial myocardium and how fibrotic patches can facilitate not only electrical but also mechanical dysfunction.

2 Methods

2.1 3D Atrial Datasets

The EP simulations were performed using the 3D atrial geometry reconstructed from the Visible Female Dataset (Figure 1a). The resolution of the latter images is 0.3 x 0.3 x 0.3 mm^3. In addition, detailed orientation of atrial fibers was included into the 3D models, as illustrated in Figure 1b. Such orientation has been previously introduced using a rule-based approach [7]. Fibrosis distributions were derived from late gadolinium enhanced magnetic resonance images (LGE MRI); such a distribution can be seen in Figure 1c. Fibrosis was segmented based on the image intensity ratio (IIR), computed by dividing individual voxel intensities by the mean blood pool intensity. Transition from diffuse to dense fibrosis was represented by labelling segmented fibrotic tissue from 1 to 5 according to LGE MRI intensity, where level 5 corresponded to dense fibrosis (IIR > 1.32) and level 1-4 corresponded to variable degree of diffuse fibrosis (1.08 < IIR < 1.32 split into four equal intervals). Fibrotic patches were then mapped into the 3D atrial geometry [5] to evaluate their role in the genesis of AF.

Mechanical simulations were performed on a tetrahedral 3D mesh with 394598 elements, derived from the 3D atrial geometry (Figure 1d). Such a mesh was generated by using iso2mesh toolbox in Matlab [8]. The average edge length was 3.8 mm. All the relevant data, including fiber orientation and fibrosis (translating into EP and mechanical tissue properties, see below), as well as simulated activation times, were mapped onto the mesh.

2.2 Modelling Atrial Electrics and Mechanics

EM coupling simulations were performed by solving the two problems independently, EP and then mechanics, using the models described below. This involved simulating AP propagation in the 3D atrial geometry first, so that the atrial activation sequences could then be mapped on the respective 3D mesh and used to simulate the resulting mechanics.

Atrial AP propagation was modelled using the standard reaction-diffusion equation:

$$\frac{\partial V}{\partial t} = \nabla \cdot (D\nabla V) + \frac{I_{tot}}{C_m} \quad (1)$$

Here V represents the cell membrane potential, I_{tot} is the total membrane ionic current and C_m is the membrane capacitance. Courtemanche-Ramirez-Nattel (CRN) model was used to describe all the main currents characterizing atrial myocytes [9]. The CRN model was solved numerically using forward Euler method on the 3D human atrial geometry with zero-flux boundary conditions. The spatial and temporal steps were 0.3 mm and 0.005 ms, respectively.

Atrial mechanics was modelled using a reduced, nearly-incompressible version of Holzapfel-Ogden (HO) formulation [10] developed previously to describe the Cauchy stress tensor in the ventricular myocardium:

$$\boldsymbol{\sigma} = a\, e^{b(I_1-3)}\, \mathbf{B} + K J(J-1)\, \mathbf{I} + 2a_f\left(I_{4f}-1\right)e^{b_f\left(I_{4f}-1\right)^2} (\boldsymbol{f} \otimes \boldsymbol{f}) + T_a(t)\, (\boldsymbol{f} \otimes \boldsymbol{f}) \quad (2)$$

Here I_1 and I_{4f} (first and fourth invariant of the Right Cauchy Green strain **C)** describe the non-muscular matrix surrounding the fibres and the fibre direction respectively; $\boldsymbol{f}$ represents the fibre field and $T_a(t)$ the active component, dependent on activation times and fiber orientation.

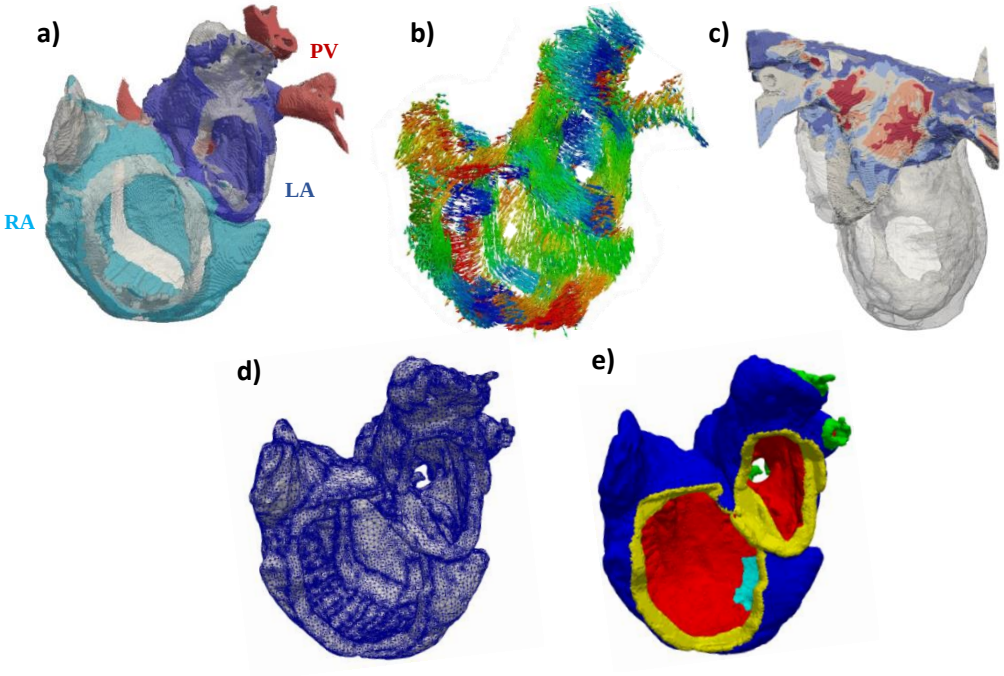

Fig. 1. 3D atrial datasets used for EP and mechanical simulations. a) 3D atrial geometry; right atrium (RA), left atrium (LA) and pulmonary veins (PVs) are shown; b) atrial fibre orientation; c) distribution of fibrosis in the 3D atria. Level of fibrosis in the LA gradually changes from high (dark red) to low (dark blue); the rest is healthy tissue (grey); d) 3D atrial mesh used for mechanics simulations; e) mesh surface boundaries, derived from the segmentation shown in a). Red: Endocardium, Blue: Epicardium, Yellow: Atrio-Ventricular Rings, Light Blue: Superior and Inferior Vena Cava, Green: PVs.

The quasi-static conservation of momentum ($\boldsymbol{\nabla} \cdot \boldsymbol{\sigma} = \mathbf{0}$) was solved throughout the cardiac cycle. Zero Dirichlet conditions were set on the valve rings and inlet veins feeding

both atrial chambers. Pressure boundary conditions were imposed on the interior of the atria based on clinically observed pressures [11–13] and zero Neumann conditions were applied on epicardial surfaces (see Figure 1e). Contraction was timed based on active potential depolarization at each point in the atrial tissue, and ran along fibers distributed throughout the model. Displacements were then solved using linear tetrahedral finite elements using the multi-physics solver, CHeart [14].

2.3 Atrial EM coupling simulations

EP simulations were performed for three different conditions: (i) sinus rhythm (SR) simulated as normal atrial activations following a stimulus applied in the SAN, (ii) functional re-entry simulated by applying cross-field protocol in the right atrium (RA) and (iii) structural re-entry around fibrotic patches in left atrium (LA) generated by fast-pacing at the pulmonary veins (PVs). In the latter case, both the AP conduction velocity and atrial wall stiffness were scaled according to the LGE MRI intensity associated with the accumulation of fibrosis.

For case (i), two diffusion coefficients, D_L and D_T (elements of the diffusion tensor in Equation (1), related to longitudinal and transverse cell-to-cell coupling), were set to 0.3 mm^2 ms^{-1} and 0.03 mm^2 ms^{-1}, respectively. For case (ii), D_L and D_T were lowered to 0.12 mm^2 ms^{-1} and 0.012 mm^2 ms^{-1}, respectively. Approximately half of the wave initiated from the SAN was blocked at t = 50 ms and measurement of the activation times started at t = 240 ms and it was carried until t = 450 ms (for the duration of the whole period of re-entry). Activation times were calculated according to the steepest rate of AP change (upstroke) in the cell.

For case (iii), re-entry was facilitated by rescaling the diffusion coefficients according to the level of fibrosis [5]: level 0 corresponded to healthy tissue and D_L = 0.3 mm^2 ms^{-1}; inside the fibrotic patch, the value of D_L for levels 1 to 5 was 0.25 mm^2 ms^{-1}, 0.20 mm^2 ms^{-1}, 0.15 mm^2 ms^{-1}, 0.10 mm^2 ms^{-1} and 0.05 mm^2 ms^{-1}, respectively. We did not used the value D_L = 0 for level 5, because there is no experimental evidence suggesting that dense fibrotic regions are completely non-conductive. The initial S1 stimulus was applied to the left posterior PV, and it was followed by a second S2 at t = 147 ms to initiate a rotor around the fibrotic patches.

As for the mechanical simulations, the main parameters were set to be a = 650 Pa, b = 5, a_f = 3260 Pa and b_f = 5 for all conditions by adjusting computational values used for mechanical simulations of the ventricular tissue [15]; for case (iii), $T_a(t)$ was scaled according to the LGE MRI intensity associated with the fibrotic patches (levels 1-5, see above). The reference value of $T_a(t)$ was calculated from Laplace's Law, $T_a(t) = \frac{PR}{2h}$, which approximates the geometry to a thin-walled sphere, simplifying calculation of the tangential stress acting of the walls of such a geometry. In this study, values of the atrial radius R and myocardial thickness h were taken from Pironet et al. [11]: R = 30 mm and h = 2 mm, respectively.

CHeart solver [14] was used to perform all mechanical simulations. These were run on a local cluster (32 core with AMD Opteron 6128 processors, 125Gb RAM) using 20 cores. The EP model was developed in C++ and ran on a local High Performance Computing cluster (SGI UV, 640 cores with Intel Xeon 8837 processors, 5 Tb RAM) using 128 cores. The duration of EP simulations was about 2 hours per 1 second of activity, whereas mechanical contractions were simulated in about 4 hours per atrial contraction cycle.

3 Results

3D atrial model was simulated for three cases: (i) normal atrial activation in SR (Figure 2a), (ii) functional re-entry in the RA (Figure 2b) and (iii) structural re-entry in the LA in the presence of fibrotic patches (Figure 2c). Activations in the three scenarios showed different patterns in SR and AF, with excitation waves in cases (ii) and (iii) forming rotors that persisted for several periods. The activation sequences corresponding to one period of the rotor can be seen in Figure 2b and Figure 2c, respectively, with the RA activated before the LA in the former, and the LA activated before the RA in the latter. The rotation period was around 210 ms for case (ii) and around 180 ms for case (iii). In the control condition (i), the total atrial activation time was 130 ms, with the latest activation in the RA occurring after 92 ms and the latest activation in the LA after 120 ms, as summarised in Table 1. These results are in agreement with the experimental observations by Lemery et al. [16].

Table 1. Activation times in the RA and LA for control condition and periods of re-entry during AF. The results for the control condition are compared here with the experimental results obtained by Lemery et al., whereas re-entry has been validated against clinical studies by Haïssaguerre et al [17].

	Simulated activation time	**Experiment (Lemery et al. [8])**
Latest RA (case (i))	95 ms	97 ± 17 ms
Latest LA (case (i))	120 ms	116 ± 18 ms
	Simulated rotor period	**Experiment (Haïssaguerre et al. [17])**
Structural re-entry (case (ii))	210 ms	230 ms
Functional re-entry (case (iii))	180 ms	175 ± 30 ms

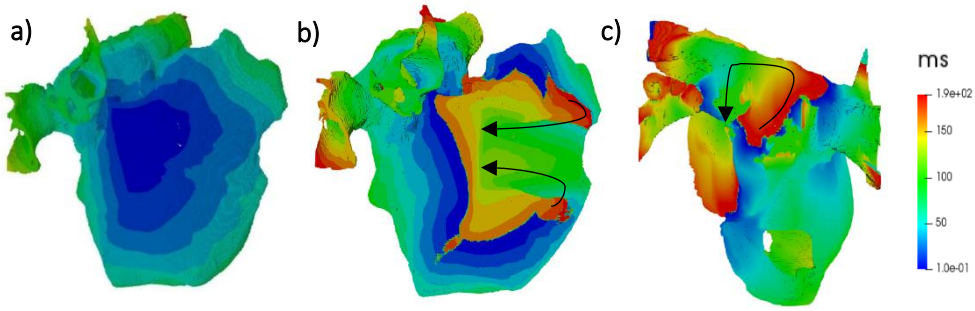

Fig. 2. Activation sequences in the 3D atrial model simulated in SR and different AF scenarios. a) control case (i); b) and c) re-entry in the RA and LA in case (ii) and (iii), respectively. Atrial activation times are shown using the rainbow palette, and the black arrows indicate the trajectories of the rotors.

Mechanical contractions in the three cases considered were also substantially different. Figure 3 shows the differences in atrial displacements between control condition (i) and case

(ii) at t = 250 ms, and Figure 4 shows the respective difference in the displacements between control condition (i) and case (iii) at t = 300 ms. The maximum relative displacements are mainly located in the RA for case (ii) and in LA for case (iii): the respective values are -5.5 mm and -5.9 mm, both showing substantially reduced contractions. Such maxima occur at around t = 250 ms in case (ii) and around t = 300 ms in case (iii). Figure 5 shows changes of the absolute displacement over the period of contraction for each of cases (i), (ii) and (iii), as well as regional differences in the magnitudes of the displacement between the LA and RA.

The major differences in contraction during re-entry for case (ii) and (iii) were seen in the RA near SAN and in the LA near fibrotic patches, respectively; these were the locations where the rotors were initiated and sustained their rotation (Figure 3 and Figure 4).

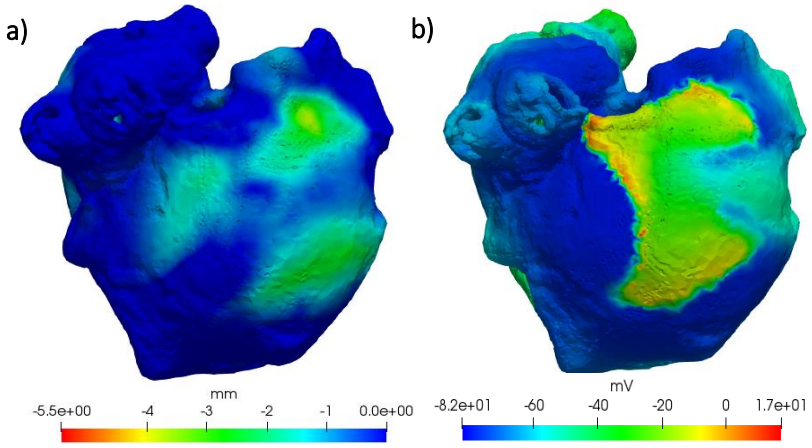

Fig. 3. a) Difference in displacement between control condition (i) and case (ii) at *t* = 250 ms. The most affected area was the RA, where the rotor was initiated and perpetuated (maximum reduction in contraction up to -5.5 mm). However, contraction of parts of LA was also affected substantially. b) shows the 3D voltage distribution at the beginning of one period of the rotor.

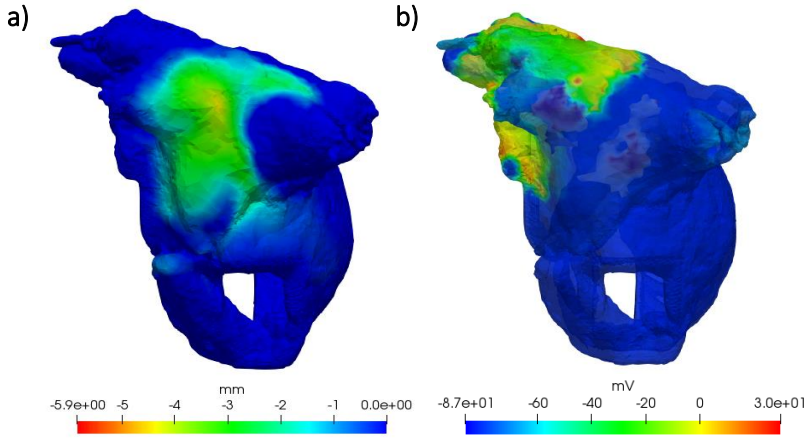

Fig. 4. a) Difference in displacement between control condition (i) and case (iii) at t = 300 ms (maximum reduction in contraction up to –5.9 mm); major differences can be seen to be around the fibrotic patches. b) shows the 3D voltage distribution half way through the period of the rotor.

The displacements at peak contraction, calculated with respect to the baseline values during the maximum expansion, are shown in Table 2 and compared with experimental values obtained by Quintana et al. [18] in healthy subjects. The values of displacements in the RA agreed with the experimental values. In the LA, the simulated results were significantly higher than experimental values [9] for case (i) and (ii). However, another study [19] reported substantially higher displacement values in the LA during contraction.

Table 2. Atrial displacement during peak contraction in the RA and LA. Results of EM simulations for cases (i) - (iii) are compared here with experimental values by Quintana et al. for healthy subjects.

	SR case (i)	**RA Re-entry case (ii)**	**LA Re-entry case (iii)**	**Experiment (Quintana et al.** [18]**)**
Posterior RA	6.8 mm	6.1 mm	6.7 mm	6.7 ± 2.3 mm
Posterior LA	7.8 mm	7.6 mm	4.5 mm	4.0 ± 0.9 mm

4 Conclusion

In this study, a novel coupled EM model of both atria was developed and applied to investigate changes in mechanical contraction from normal to abnormal electrical activity. The modelling enabled 1) simulation of mechanical contraction in the 3D atria following normal SR, with both electrophysiological and mechanistic results validated by experimental values; 2) simulation of EM coupling in the 3D atria during AF in two different scenarios (functional rotor in the RA and structural re-entry in the LA due to fibrotic tissue) and 3) identification of the differences in maximal atrial displacements between AF scenarios with respect to the normal activation: 6.1 mm (functional re-entry) against 6.8 mm (SR) in the RA near the SAN, and 4.5 mm (structural re-entry) against 7.8 mm (SR) in the LA near fibrotic patches. Hence, modelling showed that the weakest contraction occurred in the LA in presence of fibrosis.

Validation of EP results was carried by comparing activation sequences derived from the simulations with the respective experimental values obtained previously [10, 11].

Validation and interpretation of mechanical results were more challenging due to the smaller number of existing studies. Hence, our analysis focused on changes in atrial displacement during contraction in the posterior LA and RA, validating the control simulation against results of an experimental study by Quintana et al. [18], and then focusing on the difference between normal and abnormal contractions.

Novelty of this EM model lies in the introduction of fibrotic distribution and analysis of its impact on the EM coupling. A previous atrial EM model by Adeniran et al. [20] focused on the analysis of AF-induced electrical remodelling leading to impaired atrial mechanics without, however, emphasising the structural remodelling caused by fibrosis. Our study not only accounts for such structural remodelling effects, but also suggests that greatest decrease in peak displacement can be used as a biomarker to identify atrial regions where functional and structural re-entry can be located. In the future, regional peak displacements could be further analysed to produce simple binary indices for the stratification of AF patients.

Future EM models could improve on some limitations of this work by considering 1) additional effects of AF-induced remodelling [21]; 2) AF scenarios based on re-entry around the PVs [22]; 3) patient-specific MR imaging data [23] to enable clinical translation of the results and 4) other mechanical properties of the myocardium together with atrial displacements (such as strain and volume profiles). Future research could also include the mechano-electric feedback, integrate calcium dynamics to the excitation-contraction coupling model and incorporate patient-specific mechanical properties and hemodynamic effects, ultimately creating truly multi-physics models of the human atria.

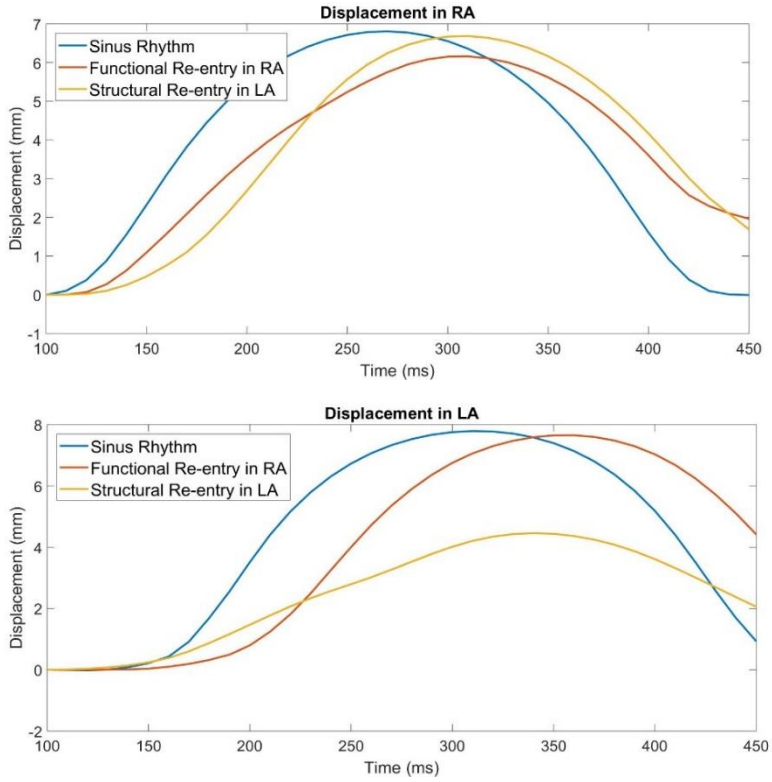

Fig. 5. Relative displacement over time during contraction in the posterior RA and posterior LA for cases (i) - (iii). Reference: maximum value of inflation.

Acknowledgements. This work was supported by the Engineering and Physical Sciences Research Council (EPSRC) [EP/L015226/1], the British Heart Foundation [PG/15/8/31138] and the Wellcome/EPSRC Centre for Medical Engineering [WT 203148/Z/16/Z].

References

1. Nattel, S.: New ideas about atrial fibrillation 50 years on. Nature. 415, 219–226 (2002)
2. Camm, A.J., Kirchhof, P., Lip, G.Y.H., Schotten, U., Savelieva, I., et al.: Guidelines for the management of atrial fibrillation. Eur. Heart J. 31, 2369–2429 (2010)
3. Ball, J., Carrington, M.J., McMurray, J.J. V, Stewart, S.: Atrial fibrillation: Profile and burden of an evolving epidemic in the 21st century. Int. J. Cardiol. 167, 1807–1824 (2013)
4. Pandit, S. V., Jalife, J.: Rotors and the dynamics of cardiac fibrillation. Circ. Res. 112, 849–862 (2013)
5. Morgan, R., Colman, M.A., Chubb, H., Seemann, G., Aslanidi, O. V: Slow Conduction in the Border Zones of Patchy Fibrosis Stabilizes the Drivers for Atrial Fibrillation: Insights from Multi-Scale Human Atrial Modeling. Front. Physiol. 7, 474 (2016)
6. Zahid, S., Cochet, H., Boyle, P.M., Schwarz, E.L., Whyte, K.N., Vigmond, E.J., Dubois, R., Hocini, M., Haissaguerre, M., Jais, P., Trayanova, N.A.: Patient-derived models link re-entrant driver localization in atrial fibrillation to fibrosis spatial pattern. Cardiovasc. Res. 110, 443–54 (2016)
7. Krueger, M.W., Schmidt, V., Tobón, C., Weber, F.M., Lorenz, C., et al.: Modeling atrial fiber orientation in patient-specific geometries: A semi-automatic rule-based approach. FIMH. 6666 LNCS, 223–232 (2011)
8. Fang, Q., Boas, D.A.: Tetrahedral mesh generation from volumetric binary and gray-scale images. Proc. Sixth IEEE Int. Conf. Symp. Biomed. Imaging From Nano to Macro. 1142–1145 (2009)
9. Courtemanche, M., Ramirez, R.J., Nattel, S.: Ionic mechanisms underlying human atrial action potential properties : insights from a mathematical model Ionic mechanisms underlying human atrial action potential properties : insights from a mathematical model. Am. Physiol. Soc. 275, H301-21 (1998)
10. Holzapfel, G.A., Ogden, R.W.: Constitutive modelling of passive myocardium. Philos Trans R. 367, 3445–3475 (2009)
11. Pironet, A., Dauby, P.C., Paeme, S., Kosta, S., Chase, J.G., Desaive, T., Kian, K., Wong, L.: Simulation of Left Atrial Function Using a Multi-Scale Model of the Cardiovascular System. PLoS One 8(6), (2013)
12. Leischik, R., Littwitz, H., Dworrak, B., Garg, P., Zhu, M., Sahn, D.J., Horlitz, M.: Echocardiographic Evaluation of Left Atrial Mechanics: Function, History, Novel Techniques, Advantages, and Pitfalls. Biomed Res. Int. 2015, 1–12 (2015)
13. Cambier, B.A., Missault, L.H., Kockx, M.M., Vandenbogaerde, J.F., Alexander, J.P.E., Taeymans, Y.M., Van Cauwelaert, P.A., Brutsaert, D.L.: Influence of the breathing mode on the time course and amplitude of the cyclic inter-atrial pressure reversal in postoperative coronary bypass surgery patients. Eur. Heart J. 14, 920–924 (1993)
14. Lee, J., Cookson, A., Roy, I., Kerfoot, E., Asner, L., Vigueras, G., Sochi, T., Deparis, S., Michler, C., Smith, N.P., Nodrsletten, D.A.: Multiphysics Computational Modeling in CHeart. SIAM J. Sci. Comput. 38, 150–178 (2016)
15. Issa, O., Peguero, J., Podesta, C., Diaz, D., De La Cruz, J., Pirela, D., Brenes, J.: Left atrial size and heart failure hospitalization in patients with diastolic dysfunction and preserved ejection fraction. J. Cardiovasc. Echogr. 27, 1 (2017)
16. Lemery, R., Birnie, D., Tang, A.S.L., Green, M., Gollob, M., Hendry, M., Lau, E.: Normal atrial activation and voltage during sinus rhythm in the human heart: An endocardial and epicardial mapping study in patients with a history of atrial fibrillation. J. Cardiovasc.

Electrophysiol. 18, 402–408 (2007)
17. Haïssaguerre, M., Jaïs, P., Shah, D.C., Takahashi, A., Hocini, M., Quiniou, G., Garrigue, S., Le Mouroux, A., Le Métayer, P., Clementy, J.: Spontaneous Initiation of Atrial Fibrillation by Ectopic Beats Originating in the Pulmonary Veins. N. Engl. J. Med. 339, 659–666 (1998)
18. Quintana, M., Lindell, P., Saha, S.K., Del Furia, F., Lind, B., Govind, S., Brodin, L.Å.: Assessment of atrial regional and global electromechanical function by tissue velocity echocardiography: A feasibility study on healthy individuals. Cardiovasc. Ultrasound. 3, 1–12 (2005)
19. Patel, A.R., Fatemi, O., Norton, P.T., West, J.J., Helms, A.S., Kramer, C.M., Ferguson, J.D.: Cardiac cycle-dependent left atrial dynamics: implications for catheter ablation of atrial fibrillation. Hear. Rhythm. 5, 787–93 (2008)
20. Adeniran, I., Maciver, D.H., Garratt, C.J., Ye, J., Hancox, J.C., Zhang, H.: Effects of persistent atrial fibrillation- induced electrical remodeling on atrial electro-mechanics - insights from a 3D model of the human atria. PLoS One. 10, (2015)
21. Colman, M.A., Aslanidi, O. V, Kharche, S., Boyett, M.R., Garratt, C., Hancox, J.C., Zhang, H.: Pro-arrhythmogenic effects of atrial fibrillation-induced electrical remodelling: insights from the three-dimensional virtual human atria. J. Physiol. 591, 4249–72 (2013)
22. Aslanidi, O. V, Colman, M.A., Varela, M., Zhao, J., Smaill, B.H., Hancox, J.C., Boyett, M.R., Zhang, H.: Heterogeneous and anisotropic integrative model of pulmonary veins: computational study of arrhythmogenic substrate for atrial fibrillation. Interface Focus. 3, 20120069 (2013)
23. Varela, M., Morgan, R., Theron, A., DIllon-Murphy, D., Chubb, H., Whitaker, J., Henningsson, M., Aljabar, P., Scherffter, T., Kolbitsch, C., Aslanidi, O. V: Novel MRI Technique Enables Non-Invasive Measurement of Atrial Wall Thickness. IEEE Trans. Med. Imaging. 36, 1607–1614 (2017)